Nanoscale

PAPER

View Article Online
View Journal | View Issue

Cite this: *Nanoscale*, 2026, **18**, 5799

Noble-metal-free, atomically thin $CuInP_2N_x$ nanosheets as highly efficient, stable, and low-cost electrocatalysts in acid oxygen evolution reactions

Wentao Hou,[a] Xin Zhou, *[b,c] Tingting Cheng,[a] Haoqiang Chi,[a] Yongcai Zhang, [d] Chen Zhuang,[a] Yubin Zheng,[a] Xiaohui Zhong, *[e] Zhigang Zou[a,f] and Yong Zhou *[a,f]

Received 20th November 2025,
Accepted 3rd February 2026

DOI: 10.1039/d5nr04906g

rsc.li/nanoscale

Highly active and durable electrocatalysts for the oxygen evolution reaction (OER) in acidic conditions are highly desired for renewable energy nowadays. In this work, a new type of noble-metal-free, atomically thin $CuInP_2N_x$ nanosheets was synthesized through the facile nitridation of the corresponding $CuInP_2S_6$ and utilized for electrocatalytic water splitting. The combined merits of metal nitrides and the 2D morphology improved the OER performance, achieving an overpotential of 356 mV at a current density of 10 mA cm^{-2} and a long-term durability of 60 h in 0.5 M H_2SO_4 electrolyte. The changes in the electronic structure with the introduction of N in $CuInP_2N_x$ efficiently lower the energy barriers of intermediates, especially those of OH* and OOH*, thus causing the OER process to be more thermodynamically favourable. This work may provide inspiration for the exploration of cost-effective, novel transition-metal nitride catalysts with excellent OER performance and stability.

The exploitation of green, renewable energy has been rapidly advancing in recent years because of the urgency to solve energy and environmental issues.[1,2] Compared with harvesting, the storage and utilization of these energies are much more difficult owing to their intermittent nature.[3,4] The electrocatalytic oxygen evolution reaction (OER) enables energy conversion to stable chemical energy and presents a practical strategy for addressing these challenges.[5,6] The OER in acidic electrolytes is preferred to that in alkaline electrolytes in proton exchange membrane water electrolyzers (PEMWEs) and has attracted more research attention recently.[7] To overcome the high overpotential caused by the thermodynamically uphill nature and sluggish kinetics of the OER process, the key objective is to design and synthesize efficient catalysts.[8] The electrocatalyst must also exhibit great stability in harsh acidic environments to ensure its long-term use.[9]

Nowadays, iridium (Ir)- and ruthenium (Ru)-based materials are the main electrocatalysts in commercial, scalable OER reactions, while Ir-based materials seem to be the only choice when it comes to acidic environments.[10] Despite exhibiting great OER performances, these noble-metal-based catalysts suffer from relatively high cost and scarcity of raw materials, severely restricting their large-scale applications.[11] Thus, developing new noble-metal-free electrocatalysts with moderate cost, excellent performance, and reliable stability has been a hot topic in acidic OER research.

Materials with 2D atomic structures have recently emerged as new catalysts with excellent electrocatalytic performances,[12–15] offering great prospects for application in the acidic OER process. Their distinct properties compared with their bulk counterparts are mainly attributed to the following: (1) the ultrathin structure effectively shortens the diffusion pathway to the surface, facilitating the transfer of charge carriers and mass exchange; (2) the increased specific surface area allows sufficient exposure to the electrolytes, providing rich active sites for the OER. More importantly, it is convenient to modify 2D materials, such as creating vacancies and

[a]*School of Physics, Jiangsu Key Laboratory of Nanotechnology, Eco-materials and Renewable Energy Research Center (ERERC), National Laboratory of Solid-State Microstructures, Collaborative Innovation Center of Advanced Microstructures, Nanjing University, Nanjing, Jiangsu, 210093, P. R. China. E-mail: zhouyong1999@nju.edu.cn*
[b]*Interdisciplinary Research Center for Biology and Chemistry, Liaoning Normal University, Dalian, Liaoning, 116029, P. R. China. E-mail: zhouxin@dlu.edu.cn*
[c]*College of Environment and Chemical Engineering, Dalian University, Dalian, Liaoning, 116622, P. R. China*
[d]*School of Chemistry and Chemical Engineering, Yangzhou University, Yangzhou, Jiangsu, 225009, P. R. China*
[e]*School of Chemical and Environmental Engineering, Anhui Polytechnic University, Wuhu, Anhui, 241000, P. R. China. E-mail: zxhui@ahpu.edu.cn*
[f]*School of Science and Engineering, The Chinese University of Hong Kong (Shenzhen), Shenzhen, Guangdong, 518172, P. R. China*

doping, thereby enabling the tunability of properties for different applications.[16] Among the 2D electrocatalytic materials, metal nitrides have been extensively studied due to their good chemical stability and electrical conductivity.[17] The introduction of nitrogen is known to change the electronic structure of host materials by altering the carrier transmission paths or crystal structures.[18] After the nitrogen atom modification, the enhanced electrical conductivity and stability of functional materials make them highly compatible with the requirements of the acidic OER. Benefitting from the advantages of 2D nanostructures and metal nitrides, atomically thin metal nitrides could be potential OER catalysts with good performance and moderate cost.

Herein, we report the synthesis of a new type of atomically thin transition metal phosphoronitride $CuInP_2N_x$ for acidic OER catalysis. Through nitrogen substitution of sulfur in few-layer $CuInP_2S_6$ nanosheets by nitridation in an ammonia atmosphere, the resulting $CuInP_2N_x$ nanosheets exhibit high electrocatalytic performance with a lower overpotential of 356 mV at a current density of 10 mA cm^{-2} in 0.5 M H_2SO_4 electrolyte, a smaller Tafel slope of 159 mV dec^{-1}, and long-term durability of 60 h, comparable to commercial IrO_2 particles. Density functional theory (DFT) calculations indicate that the changes in the electronic structures of $CuInP_2N_x$ by the introduction of N can effectively reduce the formation energy barriers of OH* and OOH* intermediates, thus causing the OER process to be thermodynamically more favourable. This work sheds light on a facile and low-cost method for the exploration of transition-metal nitrides with improved performance and stability for various electrocatalytic applications.

The various atomically thin $CuInP_2N_x$ nanosheets were synthesized through a top-down nitrogen substitution of sulfur in few-layer $CuInP_2S_6$ by nitridation in ammonia atmosphere at different temperatures, which is described in detail in the SI. A reductive NH_3 atmosphere was chosen to accomplish the substitution of S by N atoms.[19]

Few-layer $CuInP_2S_6$ nanosheets were first fabricated through the exfoliation of bulk $CuInP_2S_6$ crystals, as demonstrated in our previous work.[20] From XRD patterns (Fig. S1), stronger (002) and (004) signals can be observed compared to bulk counterparts for few-layer $CuInP_2S_6$, indicating the well-preserved main phase and the orientation of exfoliation along the [001] direction.[21] The ultrathin structures of $CuInP_2S_6$ nanosheets were further confirmed by TEM images, as shown in Fig. S2. An obvious Tyndall effect can be observed in the ethanol dispersion of exfoliated $CuInP_2S_6$, indicating its high dispersibility brought by the ultrathin structures (Fig. S3).

Different $CuInP_2N_x$ nanosheet samples were prepared by changing the temperatures of the nitridation process. Fig. 1 displays the micromorphology of $CuInP_2N_x$-300, showing that the nanosheet structures can be well preserved with sulfur removed. The extremely low contrast indicates the ultrathin nature of $CuInP_2N_x$-300 in the SEM image (Fig. 1a). From the TEM images (Fig. 1b and c), the preservation of few-layer structures can be clearly confirmed. In high-resolution TEM images (Fig. 1d), fringes with an interplanar distance of 0.30 nm can

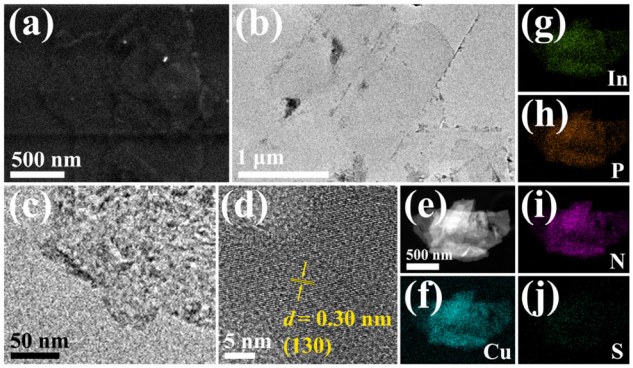

Fig. 1 (a) SEM image, (b–d) TEM and HRTEM images and (e–j) EDX elemental mapping of $CuInP_2N_x$-300.

be indexed to the (130) planes of $CuInP_2S_6$,[22] verifying the unbroken main structures after ammoniation treatment in $CuInP_2N_x$-300. This is consistent with the XRD pattern of $CuInP_2N_x$-300 (Fig. S1), in which diffraction peaks assigned to the (002), (004), (130), (−204) and (060) planes can still be confirmed. In addition, the Cu, In, P, and N elements are uniformly distributed in the EDX mapping of $CuInP_2N_x$-300, with a trace amount of S, indicating the successful substitution of sulfur by nitrogen after the ammoniation treatment (Fig. 1e–j). When the ammoniating temperature increased to 400 °C or 500 °C, the $CuInP_2N_x$ samples became aggregated and the 2D structures were destroyed, thus negatively impacting the OER performance (Fig. S4).

X-ray photoelectron spectroscopy (XPS) of samples was carried out to reveal the changes in the elemental composition and chemical states after ammoniation treatment (Fig. S5a). As shown in the total survey (Fig. S5c), signals of Cu, In, P and S were clearly defined in pristine $CuInP_2S_6$. In addition to Cu, In, and P, the N 1s peak around 400 eV was also observed in the survey XPS of $CuInP_2N_x$-300, further confirming its successful amination. The Cu 2p fine spectrum showed a pair of characteristic doublets at binding energies of 932.4 eV and 952.2 eV (Fig. 2a). No observed satellite peaks, along with the Auger peak at the kinetic energy of 917.1 eV (Fig. S5b), indicated the Cu^+ state in both $CuInP_2S_6$ and $CuInP_2N_x$-300.[23] For In 3d fine spectra (Fig. 2b), both $CuInP_2S_6$ and $CuInP_2N_x$-300 showed similar signals located at 445.3 eV and 452.8 eV, which can be indexed to In^{3+} $3d_{3/2}$ and $3d_{5/2}$, respectively.[24] Notably, clear shifts towards higher binding energy for both Cu 2p and In 3d were observed for $CuInP_2N_x$-300 (0.43 eV for Cu, 0.45 eV for In), indicating the withdrawal of electron density from both Cu and In. Such a phenomenon is due to the formation of Cu–N and In–N coordination, owing to the higher electronegativity of nitrogen compared with sulfur. After the ammonia treatment, the P 2p spectrum of $CuInP_2N_x$-300 showed an obvious shift of 1.48 eV towards higher binding energy (Fig. 2c), indicating the coordination change from P–S to the P–N bond for P atoms. S 2p signals can only be clearly observed in $CuInP_2S_6$, which contained two peaks at binding energies of 161.8 eV and 163.4 eV, assigned to $2p_{1/2}$ and $2p_{3/2}$ states of S^{2-} from the

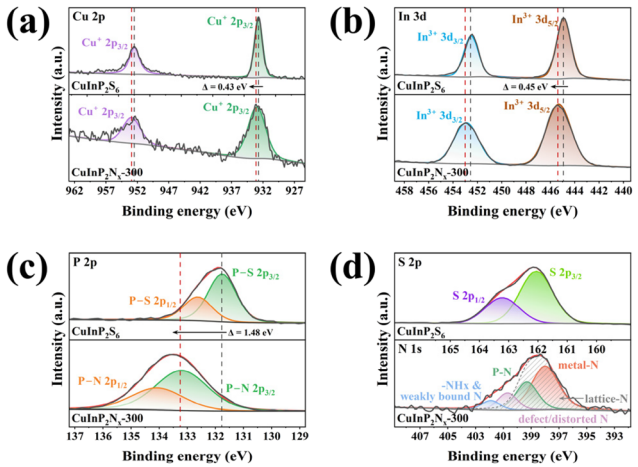

Fig. 2 High-resolution XPS spectra of $CuInP_2S_6$ and $CuInP_2N_x$-300: (a) Cu 2p, (b) In 3d, (c) P 2p, and (d) S 2p of $CuInP_2S_6$ and N 1s of $CuInP_2N_x$-300.

S–P bond (Fig. 2d).[25] For N 1s in the target $CuInP_2N_x$-300, the spectrum can be deconvoluted into four components, showing the coexistence of multiple chemical states (Fig. 2d). The main peak at a relatively low binding energy of 398.0 eV is assigned to the nitrogen bonded with the Cu and In atoms. Because Cu–N and In–N bonds exhibit similar electronegativity and close binding energies, these two contributions cannot be reliably distinguished and are therefore treated as a single lattice metal–N component. The second peak at 399.2 eV can be attributed to regular lattice P–N bonding. An intermediate peak at 400.7 eV was assigned to defect- or distortion-related P–N environments, which are likely associated with local structural distortion and incomplete substitution of the S site by N, as supported by the XPS quantitative analysis in Table S3. The weak peak at a relatively high binding energy of 401.8 eV is attributed to surface $-NH_x$ species or weakly bound nitrogen introduced during the ammoniation process.[26] The dominance of lattice-N components (metal–N and P–N) of N 1s, along with the positive shifts of Cu 2p and In 3d, indicates that nitrogen is mainly incorporated into the lattice rather than adsorbed or weakly bonded on the surface in $CuInP_2N_x$-300.

Quantitative analysis of elements before and after ammoniation treatment (Tables S1–5) was conducted to reveal the change in the degree of S substitution with the increase in the ammoniation temperature. The atomic ratios of Cu, In and P for both $CuInP_2S_6$ and all $CuInP_2N_x$ samples remained close to 1 : 1 : 2, reflecting the integrity of the lattice structure. The decrease in S and increase in N contents in $CuInP_2N_x$ samples demonstrated the substitution of the S element *via* the ammoniation process. Atomic ratios of S and N in $CuInP_2N_x$-200 were approximately 12.3% and 27.3% (S : N ≈ 1 : 2.2). The S content in $CuInP_2N_x$-200 remained significant (12.29%), while the N content (27.33%) was considerably lower than in other $CuInP_2N_x$ samples, indicating that 200 °C is insufficient for substantial S substitution. For $CuInP_2N_x$-300, the S content was reduced to 3.3%, showing nearly complete substitution by N element. For samples treated at higher ammoniation temperatures (400 °C and 500 °C), no significant changes in S and N contents occurred (~3% for S, ~44% for N), showing that the substitution process is essentially complete at 300 °C. In addition, the trace amount of S element remaining in $CuInP_2N_x$-300 is due to the S residual binding with N atoms through S–N bonds during the ammoniation process. Thus, it can be concluded that the target $CuInP_2N_x$-300 was successfully synthesized through the ammoniation process.

The electrochemical OER performances of samples were investigated in 0.5 M H_2SO_4 solution using a rotating disk electrode (RDE). Performances of commercial IrO_2 particles were also tested for comparison. The linear sweep voltammetry (LSV) curves of samples were tested with a 90% iR compensation, as shown in Fig. 3a. Pristine $CuInP_2S_6$ showed very poor OER activity, which could not reach a current density of 10 mA cm^{-2} within the tested potential window. This is attributed to the intrinsic low electronic conductivity and large energy barrier for intermediate adsorption, resulting in sluggish reaction kinetics.[27,28] After ammoniation treatment at different temperatures, the overpotentials of all $CuInP_2N_x$ samples were greatly reduced, in which $CuInP_2N_x$-300 exhibited the best performance with the lowest overpotential of 356 mV at 10 mA cm^{-2} (Fig. 3b). Meanwhile, the Tafel slope of $CuInP_2N_x$-300 decreased to 159 mV dec^{-1}, indicating much faster reaction kinetics compared to $CuInP_2S_6$ (Fig. 3c).[29] It

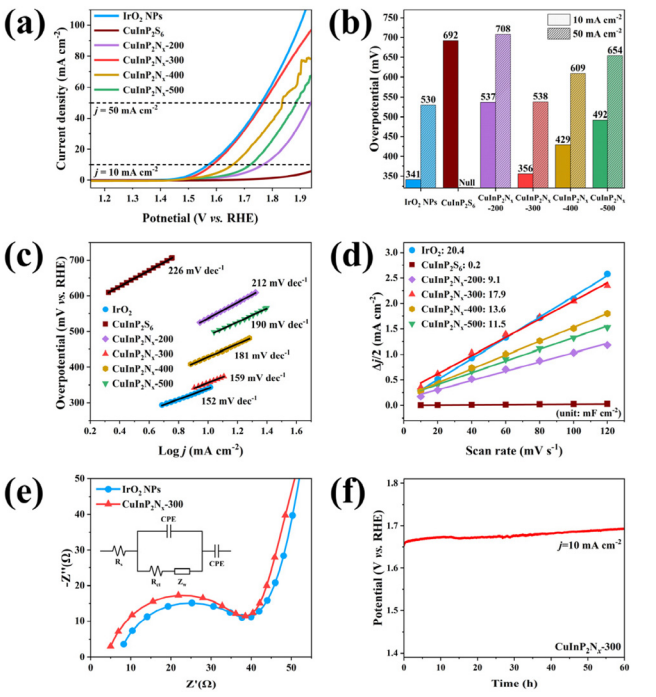

Fig. 3 Comparison of the OER performances of the prepared samples: (a) iR-compensated linear sweep voltammetry (LSV) curves, (b) overpotential at current densities of 10 and 50 mA cm^{-2}, (c) Tafel Slopes, (d) calculated double-layer capacitance (C_{dl}), and (e) electrochemical impedance spectroscopy (EIS) of $CuInP_2S_6$ and $CuInP_2N_x$-300. (f) Long-term stability of $CuInP_2N_x$-300.

should be noticed that the low overpotential of $CuInP_2N_x$-300 (356 mV at 10 mA cm^{-2} and 538 mV at 50 mA cm^{-2}) is comparable to that of commercial IrO_2 particles, showing good OER activity and potential in practical use. Besides, the excellent OER performance displayed by $CuInP_2N_x$-300 in 0.5 M H_2SO_4 is competitive with other recently reported works (Table S6).

Further, the double-layer capacitance (C_{dl}) was tested to evaluate the electrochemically active surface area (ECSA) of the samples.[30] Cyclic voltammetry (CV) curves conducted in a non-faradaic region at different scan rates (Fig. S6) showed that the C_{dl} of all $CuInP_2N_x$ samples exhibited significant increases (Fig. 3d). Among all the $CuInP_2N_x$ samples, $CuInP_2N_x$-300 exhibited the largest ECSA of 447 (Fig. S7), indicating a significantly increased electrochemically accessible surface area brought about by the N substitution. Both lower (200 °C) and higher ammoniation temperatures (400 °C and 500 °C) led to reduced ECSA, suggesting that excessive or insufficient ammoniation is unfavorable for maximizing the exposure of the active surface. Electrochemical impedance spectroscopy (EIS) of samples was also conducted to reveal the changes in the transfer kinetics after *N*-substitution. An equivalent circuit consisting of the solution resistance in series (R_s), charge transfer resistance (R_{ct}) and constant phase element (CPE) was employed to fit the Nyquist curves, as depicted in the inset of Fig. 3e. In the Nyquist curves (Fig. 3e), the radius of the semicircle in the high-frequency region represents the charge transfer resistance (R_{ct}) for electrodes.[31] Similar to commercial IrO_2, $CuInP_2N_x$-300 samples showed a small R_{ct} of 33.8 Ω, which was significantly reduced compared to that of pristine $CuInP_2S_6$ (Table S7). This indicates that N substitution can result in a much faster pathway for charge and mass exchange between the electrode and electrolyte in $CuInP_2N_x$-300 samples,[32] which is attributed to the changes in the electronic structures and is crucial for the OER process.

The long-term electrocatalytic stability is another key factor for practical application, especially in harsh acidic OER conditions.[33] As shown in Fig. 3f, the $CuInP_2N_x$-300 exhibited good electrocatalytic stability over 60 h without obvious attenuation. By comparison, the commercial IrO_2 showed an obvious decay in performance within only 6 h with a gradual increase in the overpotential (Fig. S9), which is due to the loss of active sites by dissolution.[34] This remarkable durability of $CuInP_2N_x$-300 arises from the high chemical stability of nitrides, which helps to maintain its structural integrity in the OER process.

Density functional theory (DFT) calculations were conducted to illustrate the enhancement of the OER performance of $CuInP_2N_x$. Supported by the enhanced (002) signal in the XRD pattern (Fig. S1) and the (130) planes observed in the HRTEM image (Fig. 1d), the (001) plane was selected as the basal plane for investigating OER catalytic behavior, which corresponds to the naturally exposed surface of $CuInP_2S_6$ after exfoliation. The optimized single-layer (001) surfaces of $CuInP_2S_6$ and $CuInP_2N_x$ are depicted in Fig. 4a and b. Based on the relaxed structures, the total and partial density of states (DOS) of $CuInP_2S_6$ and $CuInP_2N_x$ were calculated using the HSE06 method (Fig. 4c and d). This shows that the introduction of N can significantly alter the electronic structures of $CuInP_2N_x$. The valence band maximum (VBM) of $CuInP_2S_6$ is primarily a hybrid of Cu 3d and S 3p states, while the conduction band minimum (CBM) is dominated by a mixture of In 5s and S 3p states. In contrast, the VBM of $CuInP_2N_x$ consists mainly of Cu 3d and N 2p states, whereas the CBM is largely contributed by In 5s and N 2p states. It can be clearly seen that the main peak shifts towards the Fermi level (0 eV) after the N substitution, compared to pristine $CuInP_2S_6$, which improves the electronic conductivity in $CuInP_2N_x$.[35] Moreover, N 2p contributes to a higher density of states across the Fermi level, which means that the $CuInP_2N_x$ exhibits a more metallic nature,[36] in agreement with the decreased R_{ct} of $CuInP_2N_x$-300 in Nyquist plots (Fig. 3e). Therefore, the modulation of the electronic structures by N atoms is favourable for the adsorption of radicals such as OH*, thus facilitating the OER reactions.

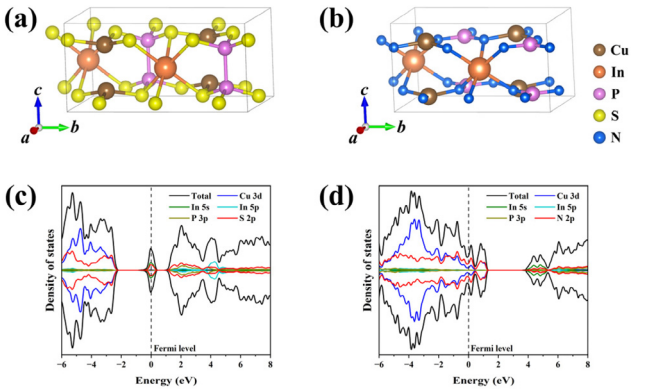

Fig. 4 DFT calculations: optimized structures of the (001) planes of (a) $CuInP_2S_6$ and (b) $CuInP_2N_x$ and the density of states (DOS) of (c) $CuInP_2S_6$ and (d) $CuInP_2N_x$.

Further, Gibbs free energies (ΔG) of intermediates were calculated to study the energy barriers during acidic OER pathways. A conventional adsorbate evolution mechanism (AEM) was considered, in which H_2O molecules go through a four-electron transfer pathway for O_2 molecule generation.[6] In such a process, intermediates of OH*, O* and OOH* are formed successively during H_2O oxidization, while O_2 and protons (H^+) are formed in acidic H_2SO_4. The detailed reaction steps are described as follows:

$$H_2O + * \rightarrow OH^* + H^+ + e^- \quad (1)$$

$$OH^* \rightarrow O^* + H^+ + e^- \quad (2)$$

$$H_2O + O^* \rightarrow OOH^* + H^+ + e^- \quad (3)$$

$$OOH^* \rightarrow * + O_2 + H^+ + e^- \quad (4)$$

where * denotes an active site on the surface of the catalysts, while OH*, O* and OOH* refer to the adsorbed intermediates during the OER process, respectively. The relaxed structures of OH*, O* and OOH* intermediates during the OER process were constructed and optimized, and the corresponding Gibbs

free energy changes of four elementary steps at pH = 0, T = 298 K and U = 0 V were calculated and drawn as shown in Fig. 5a. For pristine $CuInP_2S_6$, the calculation results show that the pathway with the lowest energy barrier is located on the S site, meaning that it is the possible active site. After N substitution of S atoms, the reaction site is altered to the more stable P site, facilitating the OER process and long-term stability. The results reveal that without applied bias, all the steps in the studied terminations are energetically uphill. The step for obtaining the OOH* intermediate undergoes the largest energy increase, which means it is the rate-determining step (RDS) for both $CuInP_2S_6$ and $CuInP_2N_x$.[37] Energy of 2.92 eV is required for the O* to OOH* conversion on pristine $CuInP_2S_6$, while a much lower energy of 2.17 eV is required on *N*-substituted $CuInP_2N_x$. This suggests that with similar O* binding strength, $CuInP_2N_x$ possesses a much stronger electron-extracting ability, which accelerates the O* oxidation in the RDS step. In addition, the energy barrier is lowered from 1.36 eV to 0.33 eV for the oxidation of H_2O molecules to OH* on $CuInP_2N_x$, indicating the facilitated H_2O dissociation and promoted initialization for OER reactions. As a result, the calculated overpotentials (η^{OER}) were 1.69 V for $CuInP_2S_6$ and 0.94 V for $CuInP_2N_x$. The above results show that the introduction of N element can effectively lower the formation energies of OH* and OOH* intermediates, thus making the OER reactions thermodynamically more favorable on $CuInP_2N_x$ than on $CuInP_2S_6$ (Fig. 5b), in good agreement with the experimental results.

In conclusion, a new noble-metal-free, atomically thin $CuInP_2N_x$ catalyst was synthesized through the simple nitridation treatment of $CuInP_2S_6$ for acidic OER applications. Combining the structural advantages of the 2D morphology and metal nitrides, the synthesized $CuInP_2N_x$ possesses abundant exposed sites, improved electronic structures, and good stability. As a result, $CuInP_2N_x$-300 nanosheets exhibit an overpotential of 356 mV at a current density of 10 mA cm^{-2}, which is comparable to commercial IrO_2 particles. The $CuInP_2N_x$-300 also exhibits long-term stability of over 60 h, endowing it with great potential for practical applications. DFT calculations show that the changes in electronic structures with the introduction of N in $CuInP_2N_x$ can efficiently lower the energy barriers of intermediates, especially the OH* and OOH*. This work can provide inspiration in preparing cost-friendly, novel transition-metal nitride catalysts with good OER performance and stability.

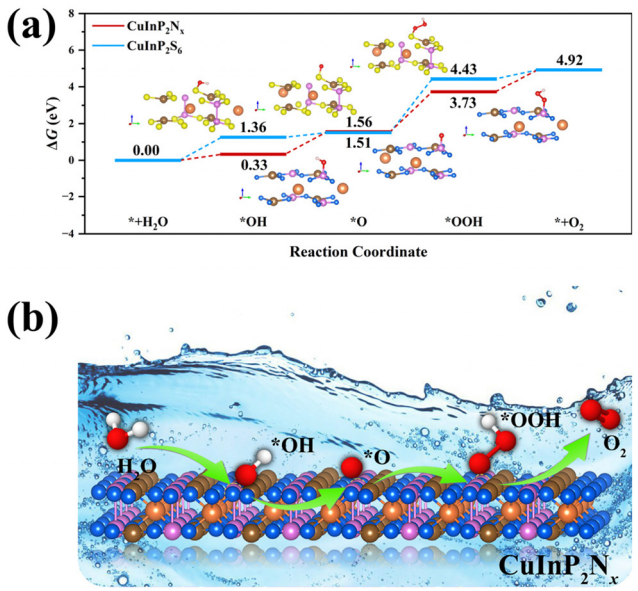

Fig. 5 (a) Gibbs free energy diagram for the OER on the $CuInP_2S_6$ (001) and $CuInP_2N_x$ (001) planes. (b) Schematic of the OER pathway on $CuInP_2N_x$.

Conflicts of interest

No conflicts of interest are to be declared in this work.

Data availability

The data included in this study are available from the corresponding author upon reasonable request. Supplementary information (SI): Experimental details and theoretical calculations and so on. See DOI: https://doi.org/10.1039/d5nr04906g.

Acknowledgements

The authors gratefully acknowledge the support of the National Key R&D Program of China (No. 2024YFB4609400), the National Natural Science Foundation of China (No. 224720022 and 22372017), the Program from Guangdong Introducing Innovative and Entrepreneurial Teams (2019ZT08L101 and RCTDPT-2020-001), and the Shenzhen Key Laboratory of Eco-materials and Renewable Energy (ZDSYS20200922160400001).

References

1 S. Chen, T. Takata and K. Domen, *Nat. Rev. Mater.*, 2017, **2**, 17050.
2 W. Wang, X. Xu, W. Zhou and Z. Shao, *Adv. Sci.*, 2017, **4**, 1600371.
3 D. A. Elalfy, E. Gouda, M. F. Kotb, V. Bureš and B. E. Sedhom, *Energy Strategy Rev.*, 2024, **54**, 101482.
4 Y. Xu, Y. Du, H. Chen, J. Chen, T. Ding, D. Sun, D. H. Kim, Z. Lin and X. Zhou, *Chem. Soc. Rev.*, 2024, **53**, 7202–7298.
5 J. Song, C. Wei, Z. F. Huang, C. Liu, L. Zeng, X. Wang and Z. J. Xu, *Chem. Soc. Rev.*, 2020, **49**, 2196–2214.
6 Y. Zhao, D. P. Adiyeri Saseendran, C. Huang, C. A. Triana, W. R. Marks, H. Chen, H. Zhao and G. R. Patzke, *Chem. Rev.*, 2023, **123**, 6257–6358.

7 Z. Zhang, C. Jia, P. Ma, C. Feng, J. Yang, J. Huang, J. Zheng, M. Zuo, M. Liu, S. Zhou and J. Zeng, *Nat. Commun.*, 2024, **15**, 1767.
8 L. An, C. Wei, M. Lu, H. Liu, Y. Chen, G. G. Scherer, A. C. Fisher, P. Xi, Z. J. Xu and C. H. Yan, *Adv. Mater.*, 2021, **33**, e2006328.
9 R. Wan, T. Yuan, L. Wang, B. Li, M. Liu and B. Zhao, *Nat. Catal.*, 2024, **7**, 1288–1304.
10 J. Huang, C. N. Borca, T. Huthwelker, N. S. Yuzbasi, D. Baster, M. El Kazzi, C. W. Schneider, T. J. Schmidt and E. Fabbri, *Nat. Commun.*, 2024, **15**, 3067.
11 M. A. Hubert, L. A. King and T. F. Jaramillo, *ACS Energy Lett.*, 2021, **7**, 17–23.
12 L. Tang, X. Meng, D. Deng and X. Bao, *Adv. Mater.*, 2019, **31**, e1901996.
13 C. P. Wang, Y. X. Lin, L. Cui, J. Zhu and X. H. Bu, *Small*, 2023, **19**, e2207342.
14 S. Yuan, S.-Y. Pang and J. Hao, *Appl. Phys. Rev.*, 2020, **7**, 021304.
15 A. Mondal and A. Vomiero, *Adv. Funct. Mater.*, 2022, **32**, 2208994.
16 C. Feng, Z. P. Wu, K. W. Huang, J. Ye and H. Zhang, *Adv. Mater.*, 2022, **34**, e2200180.
17 P. Chen, J. Ye, H. Wang, L. Ouyang and M. Zhu, *J. Alloys Compd.*, 2021, **883**, 160833.
18 W. F. Chen, J. T. Muckerman and E. Fujita, *Chem. Commun.*, 2013, **49**, 8896–8909.
19 F. Tessier, R. Marchand and Y. Laurent, *J. Eur. Ceram. Soc.*, 1997, **17**, 1821–1829.
20 W. Gao, L. Shi, W. Hou, C. Ding, Q. Liu, R. Long, H. Chi, Y. Zhang, X. Xu, X. Ma, Z. Tang, Y. Yang, X. Wang, Q. Shen, Y. Xiong, J. Wang, Z. Zou and Y. Zhou, *Angew. Chem., Int. Ed.*, 2024, **63**, e202317852.
21 W. F. Io, M.-C. Wong, S.-Y. Pang, Y. Zhao, R. Ding, F. Guo and J. Hao, *Nano Energy*, 2022, **99**, 107371.
22 B. Lin, A. Chaturvedi, J. Di, L. You, C. Lai, R. Duan, J. Zhou, B. Xu, Z. Chen, P. Song, J. Peng, B. Ma, H. Liu, P. Meng, G. Yang, H. Zhang, Z. Liu and F. Liu, *Nano Energy*, 2020, **76**, 104972.
23 S. Y. Lee, H. Jung, N. K. Kim, H. S. Oh, B. K. Min and Y. J. Hwang, *J. Am. Chem. Soc.*, 2018, **140**, 8681–8689.
24 P. Yu, F. Wang, J. Meng, T. A. Shifa, M. G. Sendeku, J. Fang, S. Li, Z. Cheng, X. Lou and J. He, *CrystEngComm*, 2021, **23**, 591–598.
25 Y. Liu, M. Zhang, X. Qian, G. Hou, Y. Li, Y. Liu, X. Li, S. Guan, J. Chen, M. Shao and Y. Zhang, *Angew. Chem., Int. Ed.*, 2025, **64**, e202516041.
26 A. V. Naumkin, A. Kraut-Vass, S. W. Gaarenstroom and C. J. Powell, *NIST X-ray Photoelectron Spectroscopy Database*, 2012.
27 S. Wang, N. Fan, Z. Zhou, Y. Hu, Q. Hui, Q. Li, J. Xue, Z. Zhou, Z. Feng, Q. Yan, Y. Weng, R. Tang, F. Zheng, R. Fan, B. Xu, L. Fang and L. You, *ACS Appl. Mater. Interfaces*, 2022, **14**, 40126–40135.
28 G. Fu, K. Xie, B. Yan, P. Yu, X. Tan, P. Liu and G. Yang, *Small*, 2024, **20**, e2403005.
29 J. Li, D. Chu, H. Dong, D. R. Baker and R. Jiang, *J. Am. Chem. Soc.*, 2020, **142**, 50–54.
30 J. Zhang, T. Quast, W. He, S. Dieckhofer, J. R. C. Junqueira, D. Ohl, P. Wilde, D. Jambrec, Y. T. Chen and W. Schuhmann, *Adv. Mater.*, 2022, **34**, 2109108.
31 X. Xiao, D. Huang, Y. Fu, M. Wen, X. Jiang, X. Lv, M. Li, L. Gao, S. Liu, M. Wang, C. Zhao and Y. Shen, *ACS Appl. Mater. Interfaces*, 2018, **10**, 4689–4696.
32 H. Jin, J. Wang, D. Su, Z. Wei, Z. Pang and Y. Wang, *J. Am. Chem. Soc.*, 2015, **137**, 2688–2694.
33 F.-Y. Chen, Z.-Y. Wu, Z. Adler and H. Wang, *Joule*, 2021, **5**, 1704–1731.
34 P. Jovanovic, N. Hodnik, F. Ruiz-Zepeda, I. Arcon, B. Jozinovic, M. Zorko, M. Bele, M. Sala, V. S. Selih, S. Hocevar and M. Gaberscek, *J. Am. Chem. Soc.*, 2017, **139**, 12837–12846.
35 J. Yang, A. R. Mohmad, Y. Wang, R. Fullon, X. Song, F. Zhao, I. Bozkurt, M. Augustin, E. J. G. Santos, H. S. Shin, W. Zhang, D. Voiry, H. Y. Jeong and M. Chhowalla, *Nat. Mater.*, 2019, **18**, 1309–1314.
36 R. Jin, J. Huang, G. Chen, W. Chen, B. Ouyang, D. Chen, E. Kan, H. Zhu, C. Li, D. Yang and K. Ostrikov, *Chem. Eng. J.*, 2020, **402**, 126257.
37 K. Wu, L. Shi, Z. Wang, Y. Zhu, X. Tong, W. He, J. Wang, L. Zheng, Y. Kang, W. Shan, Z. Wang, A. Huang and B. Jiang, *Chem. Commun.*, 2023, **59**, 3138–3141.